Journal of Materials Chemistry A

Accepted Manuscript

ROYAL SOCIETY OF CHEMISTRY

www.rsc.org/materialsA

Amphiphilic Fullerenes Modified 1D ZnO Arrayed Nanorods-2D Graphene Hybrids as Cathode Buffer Layers for Inverted Polymer Solar Cells

Ting Hu[a], Lie Chen[a,b], Zhiqiang Deng[a], Yiwang Chen*[a,b]

[a]College of Chemistry/Institute of Polymers, Nanchang University, 999 Xuefu Avenue, Nanchang 330031, China

[b]Jiangxi Provincial Key Laboratory of New Energy Chemistry, Nanchang University, 999 Xuefu Avenue, Nanchang 330031, China

*Corresponding author. Tel.: +86 791 83968703; fax: +86 791 83969561. E-mail: ywchen@ncu.edu.cn (Y. Chen).

Abstract

Amphiphilic fullerene-end-capped poly(ethylene glycol) (C60-PEG) is synthesized to modify uniform ZnO arrayed nanorods (ANs) grown *in situ* on the surface of poly(N-vinyl pyrrolidone) decorated reduced graphene oxide (RGO). The two dimensional (2D) graphene provides a stable and conductive flat substrate for one dimensional (1D) arrayed nanorods with reduced defects. The addition of amphiphilic C60-PEG can improve the compatibility of cathode buffer layer and the active layer. Meanwhile, C60-PEG produces a modified efficacy on the arrayed nanorods with reduced defects and decreased work function. Compared to the bare ZnO ANs, C60-PEG modified ZnO ANs@RGO cathode buffer layer can reduce the recombination of carriers, increase the electron mobility and enhance electron extraction. As a result, the efficiency of the inverted polymer solar cells based on thieno[3,4-b]-thiophene/benzodithiophene (PTB7):[6,6]-phenyl-C_{71}-butyric acid methyl ester ($PC_{71}BM$) is improved to 8.1% with better long-term stability.

Keywords: Nanoarrays; Polymer solar cells; Zinc oxide; Graphene; Fullerenes

Introduction

Over the past few decades, polymer solar cells (PSCs) have drawn extensive research, owing to their potential for large area roll-to-roll manufacturing.[1, 2] Due to the hygroscopicity and acidity of poly(3,4-ethylenedioxythiophene):poly-(styrenesulfonate) (PEDOT:PSS) and the air sensitive Al cathode, the conventional PSCs behave a bad stability in air.[3-5] Therefore, the inverted PSCs is employed to solve above problems by adopting high work function metal (Au, Ag) as anode and inorganic nano-materials with high carrier mobility as buffer layer.[4, 6, 7]

The one dimensional (1D) nanostructure can promote the electron transport by providing a direct path rather than zigzag pathway compared to the zero dimensional (0D) nanostructure.[8-10] The electron mobility and the life-time of electron are proved to be increased in the 1D nanostructure.[8, 11] Besides, the arrayed nanorods also can be applied as the optical spacer to enhance the light harvesting efficiency.[12-15] Notably, zinc oxide (ZnO) is used extensively in PSCs.[16, 17] The vertically aligned ZnO arrayed nanorods have been widely employed as photo-anode, electron acceptor or buffer layer with excellent properties.[18-21] ZnO arrayed nanorods could be synthesized by hydrothermal reaction at a low temperature over a large area.[22]

Recently, graphene has been a focus for study because of its unique chemical and physic properties.[23-25] It provides a building block for the preparation of various functional composite materials. Many 2D graphene/1D nano-materials composites have been reported.[20, 26-29] Unfortunately, the strong π-stacking interactions between graphene sheets make it difficult to disperse pristine graphene in the solution, which limits its application in the optoelectronic devices. Graphene oxide (GO) is often used to replace the graphene sheets due to its good dispersion in solution. However, compared to graphene, GO has a poor conductivity with an abundance of oxygen functional groups. In order to take advantage of the conductivity, GO is usually reduced to RGO. However, a high temperature is necessary for the reduction reaction, which is also the requirement for the growth of nano-materials. Besides, when the composites are employed in the PSCs, the compatibility between organic polymer and

inorganic nano-materials should not be ignored. The inorganic buffer layer has a poor interfacial contact with the organic active layer, which lead to a bad electron extraction.[30] Therefore, the modification of the interface plays a critical role in the improvement of electron extraction.

Herein, a novel ZnO/graphene nanocomposite is developed as a cathode buffer layer to improve the performance of polymer solar cells. As we reported before,[31] ZnO nanoparticles (ZnO NPs) could grow homogenously *in situ* on the surface of poly(*N*-vinyl pyrrolidone) (PVP) decorated RGO nanosheets with less defects and traps. In this work, with the ZnO NPs as seed, uniform and vertical ZnO arrayed nanorods (ZnO ANs) are developed on the surface of PVP decorated RGO by hydrothermal method at a relatively low temperature. Compared to the pristine ZnO ANs, ZnO ANs@RGO can effectively block charge combination and enhance the electron mobility. More importantly, amphiphilic fullerene-end-capped poly(ethylene glycol) (C60-PEG) is synthesized to further modify the ZnO ANs@RGO, aiming to improve the compatibility between inorganic ZnO ANs@RGO and organic active layer. The C60-PEG also performs an effect of n-doping on the ZnO ANs@RGO. As a result, C60-PEG/ZnO ANs@RGO substantially reduces the recombination of carriers, increases the electrical conductivity and enhances electron extraction. Incorporation of the C60-PEG modified ZnO ANs@RGO as cathode buffer layer, the performance of the inverted PSCs with thieno[3,4-b]-thiophene/benzodithiophene (PTB7):[6,6]-phenyl-C_{71}-butyric acid methyl ester ($PC_{71}BM$) reaches to 8.1%, which is higher than the corresponding devices with pristine ZnO ANs of 6.9%.

Results and Discussion

The chemical structures of the materials employed for device fabrication, and the inverted device architecture with the schematic diagram of cathode buffer layer are present in **Figure 1.** GO was synthesized with a modified Hummers' method from graphite powder.[32] PVP decorated RGO was obtained by reducing GO with hydrazine and ammonia in the presence of PVP according to the literature.[33] The ZnO *in situ* grew on the surface of the PVP decorated RGO as the seed of the ZnO ANs, and the synthetic details are included in the experimental section. The effect of length of

nanorods has been reported by our group[34] and the optical length is chose in this experiment. C60-PEG was spin coated on the ZnO ANs or ZnO ANs@RGO (C60-PEG/ZnO ANs or C60-PEG/ZnO ANs@RGO). C60-PEG was synthesized by the Steglich esterification according to the literature[35] and the synthetic details are described in the experimental section. The chemical structure of C60-PEG was identified by ^{1}HNMR (**Figure S1**) and Fourier transform infrared (FT·IR) spectroscopy (**Figure S2**). The electrochemical property of C60-PEG was measured by cyclic voltammetry (**Figure S3**). C60-PEG is very stable in air and soluble in alcohols and organic solvents. In order to investigate whether the C60-PEG pile up on the top of the ZnO ANS or permeate into the space of the ZnO ANs, oxygen plasma treatment is used. C60-PEG/ZnO ANs@RGO with plasma represents that the C60-PEG modified ZnO ANs@RGO are treated by oxygen plasma processing of 10 min.

------Figure 1------

Atomic force microscopy (AFM) analysis was carried out to investigate the morphology of the samples. AFM height images of samples are shown in **Figure 2** (**a-e**). Compared with the pristine ZnO ANs growing on ITO glass (**Figure 2a**), the ZnO ANs@RGO exhibits a smoother surface with root-mean-square (RMS) roughness value of 11.08 nm (**Figure 2c**). The smoother film containing uniform ZnO ANs@RGO is attributed to the uniform ZnO seeds *in situ* growing on PVP decorated RGO, which was proved in our previous work.[31] When C60-PEG is introduced, the pristine ZnO ANs modified by C60-PEG processes the roughest surface owning to the accumulated C60-PEG on top of ZnO ANs (**Figure 2b**). However, the C60-PEG modified ZnO ANs@RGO film presents a different morphology with smoother surface (**Figure 2d**). We suppose a strong π-π interaction between graphene and C60-PEG drives the C60-PEG to permeate into the space of the ZnO ANs, and the hydrophilic side chain further facilitate the movement of the C60-PEG. The oxygen plasma treatment leads to a rougher C60-PEG/ZnO ANs@RGO film (**Figure 2e**),

which is attributed to the oxygenolysis of outside C60-PEG. In addition, due to the hydrophilia of C60-PEG, the wettability of the modified arrayed nanorods increases, as depicted in **Figure S4**. The contact angles of modified ZnO ANs and modified ZnO ANs@RGO are different, qualitatively proving that C60-PEG exists in the two samples in different forms, on the top and percolate down.

In order to get a further insight into the ZnO ANs on the RGO and the modification of C60-PEG, transmission electron microscopy (TEM) measurement was employed. As shown in **Figure 3a,** due to the lack of a holder for *in situ* growth, the pristine ZnO ANs are disordered**.** For ZnO ANs@RGO (**Figure 3b**), the ZnO ANs grew on the surface of the PVP decorated RGO (pointed by arrows**)**. The selected area electron diffraction (SAED) pattern (inset in **Figure 3b**) implies that these ZnO ANs are ordered. Moreover, the well-defined diffraction ring of with six light spots suggests that thin, flat graphene in ZnO ANs@RGO composite. In order to further reveal the detailed structure of ZnO ANs@RGO, the HRTEM images of ZnO ANs@RGO are shown in **Figure 3c** (a side elevation) and **Figure 3d** (a top view). The lattice spacing of 0.52 nm and 0.26 nm is associated with the (0001) and (0002) latticeplanes of ZnO, respectively.[36] Meanwhile, the SAED pattern (inset in **Figure 3c**) confirms that the arrayed nanorods are single crystalline and had a wurtzite-like structure. Monocrystalline and ordered ZnO arrayed nanorods could provide a direct and fast path for electron transfer, and decrease the charge recombination in the interfacial layer at the same time. The TEM images of C60-PEG modified ZnO ANs@RGO with different scales are also collected (**Figure 3e-h**). Compared with the ZnO ANs@RGO without C60-PEG (the inset of **Figure 3f**), C60-PEG modified ZnO ANs@RGO (**Figure 3e** and **f**) reveals a rough surface with black dots on the surface. The top view of C60-PEG/ZnO ANs@RGO (**Figure 3g)** shows a regular hexagon covered by something, which implies that the C60-PEG anchors on the surface of the nanorods. Besides, the HRTEM image of C60-PEG/ZnO ANs@RGO (**Figure 3h)** is consistent with that phenomenon. Meanwhile, in order to certify the superiority of ZnO ANs@RGO prepared by *in situ* growth, the ZnO nanorods are physically blend with PVP decorated RGO as a contrast experiment. As present in **Figure S5a,** the pristine

ZnO nanorods scatter in disorder. Similarly, ZnO nanorods lied intricately, not vertically growing on the surface of PVP decorated RGO (**Figure S5b**). For the modified samples, it is not obviously to observe that the C60-PEG is on the nanorods (**Figure S5c** and **d**).

To verify whether C60-PEG could improve the compatibility between inorganic ZnO ANs@RGO and organic active layer, the scanning electron microscopy (SEM) was conducted. Although the surface and cross section morphology of the pristine ZnO arrayed nanorods (**Figure 4A, a)** is similar to that of ZnO ANs@RGO (**Figure 4C, c)** with hexagon arrayed nanorods, they become quite different after modified by C60-PEG. In **Figure 4B**, the pristine ZnO arrayed nanorods retain the shape of regular hexagon after modified with C60-PEG. No significant change can be detected in the corresponding cross-sectional SEM image (**Figure 4b**). It implies that C60-PEG did not percolate down but state on the top of the arrayed nanorods. Nevertheless, the ZnO ANs@RGO changes from regular hexagon to cylinder after modified by C60-PEG (**Figure 4D** and **d**). It demonstrates that C60-PEG percolate down to the arrayed nanorods and anchor on the arrayed nanorods. The oxygen plasma treatment did not make a difference on the morphology of the C60-PEG/ZnO ANs@RGO (**Figure 4E, e**). Then, active layer was spin coated on the surface of arrayed nanorods to study the effect of C60-PEG. In order to compare the samples distinctly, the active layer is thinner than that in the device. As shown in the **Figure 4F**, the active layer coated on pristine ZnO ANs presents a film with some cracks and without any visible arrayed nanorods. Moreover, double-deck morphology can be observed obviously in the corresponding cross-sectional SEM image (**Figure 4f**). However, the arrayed nanorods can be detected under the film of active layer in the sample of C60-PEG/ZnO ANs@RGO with active layer (**Figure 4G**), and no double-deck structure are observed in the corresponding cross-sectional SEM image (**Figure 4g**). The SEM images of C60-PEG/ZnO ANs@RGO with oxygen plasma treatment (**Figure 4H, h**) present the similar morphology. This phenomenon provides the evidence that C60-PEG can improve the compatibility of inorganic ZnO ANs@RGO and organic active layer. Because of the amphipathicity property, the hydrophilic PEG

side chains anchor on ZnO and the lipophilic C60 is compatible with active layer. Therefore, C60-PEG could make the PCBM rich near the arrayed nanorods, which can facilitate the separation of excition and the transport of carriers.[37]

------Figure 2------

------Figure 3------

------Figure 4------

X-ray photoelectron spectroscopy (XPS) was applied to investigate the composition of all cathode buffer layer. As presented in **Figure 5a**, the binding energy of Zn $2p_{3/2}$ peak for ZnO ANs@RGO is located at 1021.1 eV and that for pristine ZnO arrayed nanorods is at 1020.4 eV, which are assigned to the Zn-O bonds.[38] The position of the Zn $2p_{3/2}$ peak for all the samples modified by C60-PEG shifts toward the higher binding energy in different degrees, which implies the electronic states changed as literature reported.[39, 40] C60-PEG produces an effect of n-doping on the arrayed nanorods similar with the Al-doped ZnO.[39] **Figure 5b** shows that the O 1s XPS spectra of pristine ZnO ANs and ZnO ANs@RGO are divided into two typical peaks. The peak at lower binding energy (~530.0 eV) is assigned to the Zn-O bonds.[41] The other peak at higher binding energy (531.4 eV) corresponds to oxygen atoms from hydroxyl oxygen.[41, 42] However, the O 1s XPS spectra of all the modified ZnO arrayed nanorods samples divide into two typical peaks at ~530.0 eV and ~532.3 eV. The peak at ~532.3 eV for carboxyl groups (COO-),[43] which is attributed to C60-PEG. The intensity of the peak at 530.0 eV for C60-PEG modified ZnO ANs is weaker than that of other samples. It suggests that C60-PEG accumulates on the top of the pristine ZnO ANS and the peak of Zn-O has the weakest intensity. As shown in Figure 5c, C 1s XPS spectra of all samples exhibits two peaks at ~285 eV (C–OR, R= C_2H_5) and ~288.5 eV (COOR), which is ascribed to the C atoms of carbonyl groups.[44] The extra peak at ~286.2 eV of all the modified ZnO arrayed nanorods samples for O-C-O is attributed to aromatic carbons from C60-PEG.[44, 45] The atomic concentrations of carbon, zinc and oxygen in all the samples based on the C 1s, Zn 2p and O 1s XPS spectra are summarized in **Figure 5d**. The atomic concentration of carbon from C60-PEG of C60-PEG/ZnO ANs@RGO is less than that in C60-PEG/ZnO ANs,

which suggests that C60-PEG percolate down to the ZnO@RGO arrayed nanorods. In other word, more arrayed nanorods are supposed to be exposed on the surface of C60-PEG/ZnO ANs@RGO. Therefore, the atomic concentration of zinc in C60-PEG/ZnO ANs@RGO is more than that in C60-PEG/ZnO ANs. The oxygen plasma treatment leads the oxygenolysis of C60-PEG, which make the atomic concentrations of carbon decrease. Meanwhile, the oxygen plasma treatment drives the atomic concentrations of oxygen to increase.

------Figure 5------

Since these arrayed nanorods provide the direct path for electron transport and have a high surface-to-volume ratio,[46] the photoluminescence (PL) was adopt to research the effect of PVP decorated RGO and C60-PEG on the surface defects of ZnO arrayed nanorods. The PL spectra of all samples under photoexcitation at 325 nm are displayed in **Figure 6**. The narrow emission band at 378 nm is assigned to the usual band-edge emission in the UV. However, all the spectra reveal other two emission bands in blue and green region. The peak at ~468 nm in blue regions is caused by the transitions involving Zn interstitial defect states as reported.[47] For the weak broad emission at ~525 nm in the green emission, various hypotheses have been proposed. For example, transition between singly ionized oxygen vacancies (V_o) and photoexcited holes, transition between electrons close to the conductive band and deeply trapped holes at V_o^{++}, surface defects, etc.[47-50] The two peaks about surface defects of pristine ZnO arrayed nanorods are stronger than those of other samples, and C60-PEG/ZnO ANs@RGO presents the weakest emission. It inferred that defects and traps of ZnO arrayed nanorods are passivated by PVP decorated RGO and C60-PEG, which would reduce the recombination of charge carriers.

------Figure 6------

Ultraviolet photo-electron spectroscopy (UPS) was taken to verify whether the existence of PVP decorated RGO and C60-PEG could have an effect on the work

function of the cathode buffer layer. As shown in **Figure 7a,** the left panel is E_{cutoff} gained from the high binding energy cutoff of a spectrum,[51, 52] and the right panel provides E_{onset}^{HOMO} which is the onset relative to the Fermi level (E_F) of Au (at 0 eV). The highest occupied molecular orbital (HOMO) level energies are determined according to the equation.[52]

$$E_{HOMO} = h\upsilon - (E_{onset}^{HOMO} - E_{cutoff})$$

where *hv* is the incident photon energy of 21.2 eV. Herein, the HOMO is the equal of the valence band. Consequently, the valence band (VB) for ZnO ANs, C60-PEG/ZnO ANs, ZnO ANs@RGO, C60-PEG/ZnO ANs@RGO and C60-PEG/ZnO ANs@RGO treated by plasma are -7.66 eV, -7.46 eV, -7.54 eV, -7.35 eV and -7.45 eV, respectively. By using these VB values and the optical band gap obtained from the UV–vis absorption spectra[53] (**Figure 7b**), the conduction band (CB) was calculated. The CB values for all the samples are summarized in **Table 1**. **Figure 7c** shows the corresponding energy level diagram of devices. The decreased work function could induce a better energy alignment in the device, consequently facilitating the charge extraction and collection. The better energy alignment could increase the built-in potential, which leads a higher V_{oc}.[54-56]

------Figure 7------

-------Table 1-------

Not only a good energy alignment for better charge extraction is necessary, but also a fast and stable path for electron transport is important. The space-charge-limited-current (SCLC) was employed to research the electron transporting property of ZnO nanoparticles (as a reference), ZnO ANs, C60-PEG/ZnO ANs, ZnO ANs@RGO, and C60-PEG/ZnO ANs@RGO cathode buffer layer by using electron-only devices (inset of **Figure 8**). The fitted curves using the SCLC model of all the samples are present in **Figure 8**, and the corresponding electron mobility calculated by using the Mott–Gurney SCLC equation[57, 58] are summarized in **Table 2**.

Due to the 1D nanostructure of ZnO arrayed nanorods, the electron mobility of all the arrayed nanorods samples is higher than that of ZnO nanoparticles. Thanks to the high conductive graphene, the electron mobility of ZnO ANs@RGO is further enhanced. The C60-PEG modified samples reveal a higher value than the pristine sample, and C60-PEG/ZnO ANs@RGO presents the highest electron mobility of 9.56×10^{-4} cm^2 V^{-1} s^{-1}. The electron transporting property of the ZnO nanorods/RGO prepared by physical blending was also measured. The fitted curves are displayed in **Figure S6** and the corresponding electron mobility is listed on **Table S1**. It found that the electron mobility of the blends is all lower than that of arrayed nanorods *in situ* growing on the graphene. It proves that the arrayed nanorods *in situ* growing on the graphene could produce a better path for electron transporting.

------Figure 8------

------Table 2--------

In order to further verify the optical property of ZnO ANs, the reflectance measurement was carried out to evaluate the light-trapping within the device. As displayed in **Figure 9**, all the devices using ZnO ANs as cathode buffer layer show lower reflectivity than the reference device (ZnO nanoparticles as cathode buffer layer) in the visible region and the device with C60-PEG/ZnO ANs@RGO buffer layer exhibits the lowest light reflectivity. Simultaneously, all samples show similar spectra profiles with relative high optical transmittance (**Figure S7**). It is suitable for cathode buffer layers and beneficial to improve the light absorption.

------Figure 9------

Finally, all the samples were employed as cathode buffer layer in the inverted device with the structure ITO/ cathode buffer layer/ PTB7:$PC_{71}BM$/ MoO_3/ Ag. The current density−voltage (*J-V*) curves under illuminated are shown in **Figure 10a**, while the corresponding parameters of the devices are listed in **Table 3**. The detailed preparation process of the devices is described in the experimental section. Compared to the device with bare ZnO ANs cathode buffer layer, the device with ZnO

ANs@RGO buffer layer delivers an enhanced performance, as the PCE improving from 6.9% to 7.5%. It is attributed to the high conductive graphene and the uniform ZnO ANs with high electron mobility. Notably, the device with C60-PEG/ZnO ANs@RGO buffer layer exhibits the highest PCE of 8.1% with the highest parameters, a short circuit current density (J_{sc}) of 16.25 mA cm^{-2}, an open circuit voltage (V_{oc}) of 0.737 V, a fill factor (FF) of 67.7%. The enhancement of J_{sc} and FF is attributed to a good compatibility of inorganic ZnO ANs@RGO and organic active layer after modified by C60-PEG. The IPCE spectra in **Figure 10b** are well in accordance with the J_{sc} values. As mentioned above, the improved V_{oc} results from the better energy alignment. **Figure 10c** shows the dark curve of the inverted devices**.** It was found that the leakage current of the device with C60-PEG/ZnO ANs@RGO cathode buffer layer is considerably restrained, implying that the recombination of charge was decreased.[54, 59] Furthermore, P3HT:PC_{61}BM blend was employed as active layer to verify the validity of the buffer layer (**Figure S8** and **Table S2**). Meanwhile, the devices with ZnO ANs@RGO and the C60-PEG modified ZnO ANs@RGO show a better stability than the devices with pristine ZnO (**Figure S9**). The long term stability could be attributed to the defects passivation of the ZnO by the addition of PVP decorated RGO and C60-PEG.

------Figure 10------

------Table 3------

Conclusions

In summary, ZnO ANs@RGO nanocomposites was prepared by *in situ* growing uniform and vertical ZnO arrayed nanorods on the surface of PVP decorated RGO. Amphiphilic C60-PEG was employed to further modify the ZnO ANs and improve the compatibility of cathode buffer layer and the active layer. Compared with the pristine ZnO ANs, the C60-PEG/ZnO ANs@RGO has higher electron mobility, less defects and decreased work function, which could increase the electron extraction, reduce the recombination of carriers. Consequently, incorporation of the C60-PEG modified ZnO ANs@RGO nanocomposite as cathode buffer layer can remarkably improve the performance of the inverted device.

Experimental Section

Materials

Natural graphite powder (325 mesh, Alfa-Aesar), poly(N-vinyl pyrrolidone) (PVP) (M_w=10000, Sigma-Aldrich), PEG (M_w=6000, Aladdin), poly(3-hexylthiophene) (P3HT, M_w = 60000-75000, Rieke Metals Inc), thieno[3,4-b]-thiophene/benzodithiophene (PTB7, 1-Materials), (6,6)-phenyl-C_{61} butyric acid methyl ester ($PC_{61}BM$ 99.5%; Nano-C), triphenylphosphine (>99.0%; Aladdin), [6,6]-phenyl C_{71}-butyric acid methyl ester ($PC_{71}BM$, 99%, Nano-C) and diethyl azodicarboxylate (>97.0%; Aladdin) were used as received. In addition, potassium manganeseoxide ($KMnO_4$), sulfuric acid (H_2SO_4), hydrogen peroxide (H_2O_2), hydrochloric acid (HCl) and sodium nitrate ($NaNO_3$) were of analytical purity and used as received.

Synthesis of PVP decorated graphene: GO was synthesized with a modified Hummers' method from graphite powder.[32] The PVP decorated RGO was produced according to the literature[33] as following procedures. The 30 mg GO was dispersed in 80 ml anhydrous N, N-dimethylformamide (DMF) with a continuous ultrasonication to form a homogeneous solution, followed by addition of 120 mg PVP with an extra ultrasonication. After vigorous stirring at 80 ^oC for 6 h, 10 μl of hydrazine (80% w/w) and 100 μl of ammonia solution (25% w/w) were added to the mixture followed by another stirring at 80 ºC for 2 h. The RGO remained well dispersed in DMF. Then, the result solution was centrifuged at 12000 r/min. The solid was washed several times with deionized water, then dried under vacuum for 48 h.

Synthesis of C60-PEG: First, the [6,6]-phenyl-C_{61}-butyric acid (PCBA) was obtained by the hydrolysis of PCBM according to the literature.[60] Then, PCBA (0.1 g, 0.112 mmol) and PEG (0.456 g, 0.076 mmol) were dissolved in the mixed solvent of 1,2-dichlorobenzene and methylbenzene (V:V=1:1) followed by sonication for 1 h to dissolve PCBA completely. Triphenylphosphine (0.08 g, 0.290 mmol) and the diethyl azodicarboxylate (0.055 g, 0.290 mmol) were added dropwise to the solution. The reaction was held at room temperature for 2 days. After solvent removed, the products were purified by column chromatography with ethyl acetate and methyl alcohol.

Preparation of the ZnO seed@RGO: The ZnO was synthesized following the process reported by Heeger *et al*.[4] The general procedure for the preparation of ZnO as follows. The ZnO precursor was prepared by dissolving zinc acetate dihydrate ($Zn(CH_3COO)_2{\cdot}2H_2O$, Aldrich, 99.9%, 1 g) and ethanolamine ($NH_3CH_2CH_2OH$, Aldrich, 99.5%, 0.28 g) in 2-methoxyethanol ($CH_3OCH_2CH_2OH$, Aldrich, 99.8%, 10 mL) under vigorous stirring for 12 h for the hydrolysis reaction in air. 0.7 % wt PVP decorated RGO was added to the ZnO precursor solution to obtain ZnO@RGO precursor. Then, the ZnO@RGO precursor was coat on the ITO substrate and annealed in air for 1 h at 200 ℃ to get the ZnO seed@RGO.

In situ growth of ZnO arrayed nanorods: Then the pristine ZnO seed and ZnO seed@RGO were immersed in zinc acetate and hexamethylenetetramine blended solution at 90 ℃ for 20 min by the hydrothermal method. The growth solution consisted of 50 mM (25 mL) zinc acetate and 50 mM hexamethylenetetramine (25 mL) in deionized water. The as-grown ZnO ANs were thoroughly washed with deionized water, then annealed at 200 ℃ for 1 h in air.

Fabrication of inverted polymer solar cells

ITO-coated glass substrates (35 $\Omega{\cdot}cm^{-2}$) were cleaned with alcohol, detergent, deionized water and isopropyl, and dried by nitrogen flow followed by plasma treatment for 15 minutes. All cathode buffer layers were in situ growing on the ITO-coated glass substrates. The blended solution P3HT:$PC_{61}BM$ (1:1 w/w, 1,2-dichlorobenzene, 60 °C) or PTB7:$PC_{71}BM$ (1:1.5 w/w, chlorobenzene/1,8-diiodooctane (97:3 v/v), 70 °C) was stirred in glovebox overnight, which was spin coated on top of the cathode buffer layer as active layer. Finally, anode buffer layer MoO_3 (7 nm) and anode Ag (90 nm) was deposited on the top of the active layer by thermal evaporation in a high vacuum (< 10^{-7} Torr). Current-voltage (*J-V*) characteristics were tested using Keithley 2400 Source Meter in the dark and under simulated AM 1.5 G (100 $mW{\cdot}cm^{-2}$) irradiation (Abet Solar Simulator Sun2000). Incident photon-to-current efficiency (IPCE) were measured under monochromatic illumination (Oriel Cornerstone 260 1/4 m monochromator equipped with Oriel 70613NS QTH lamp), while the calibration of the incident light

was performed with a monocrystalline silicon diode.

Characterizations

Ultraviolet–visible (UV–vis) absorption spectra and diffuse reflectance spectra were carried out by PerkinElmer Lambda 750 spectrophotometer. Hitachi F-7000 spectrofluorophotometer was applied for the measurements of photoluminescence (PL). The infrared (IR) spectra were characterized on a Shimadzu IR-Prestige-21 fourier transform infrared (FT·IR) spectrophotometer. The morphologies were measured by an atomic force microscopy (AFM, Digital Instrument Nanoscope 31), a transmission electron microscopy (TEM; JEOL JEM-2100F), and a scanning electron microscopy (SEM, FEI Quanta 200F). Ultraviolet photo-electron spectroscopy (UPS) and X-ray photoelectron spectroscopy (XPS) measurements were carried out by AXIS-ULTRA DLD spectrometer (Kratos Analytical Ltd.) using He (I) (21.2 eV) as monochromatic light source. The thickness of all the layers was measured by surface profilometry (Alpha-Step-IQ). Water contact angle measurements for all samples were taken on JC2000A contact angle instrument.

Supporting Information

The detailed experimental sections and the other characterization of devices are available. This information is available free of charge via the Internet at http://pubs.rsc.org.

Acknowledgements

This work was financially supported by the National Science Fund for Distinguished Young Scholars (51425304), National Natural Science Foundation of China (51273088, 51263016 and 51473075), National Basic Research Program of China (973 Program 2014CB260409), and Graduate Innovation Fund Projects of Jiangxi Province (YC2013-S041). Ting Hu and Lie Chen contributed equally to this work.

References

1. Y. Zhang, T. P. Basel, B. R. Gautam, X. Yang, D. J. Mascaro, F. Liu and Z. V. Vardeny, *Nat. Commun.*, 2012, **3**, 1043.
2. G. Li, R. Zhu and Y. Yang, *Nat. Photonics*, 2012, **6**, 153-161.
3. H. Yan, P. Lee, N. R. Armstrong, A. Graham, G. A. Evmenenko, P. Dutta and T. J. Marks, *J. Am. Chem. Soc.*, 2005, **127**, 3172-3183.
4. Y. Sun, J. H. Seo, C. J. Takacs, J. Seifter and A. J. Heeger, *Adv. Mater.*, 2011, **23**, 1679-1683.
5. K. Norrman, S. A. Gevorgyan and F. C. Krebs, *ACS Appl. Mater. Interfaces*, 2008, **1**, 102-112.
6. Y. Ka, E. Lee, S. Y. Park, J. Seo, D.-G. Kwon, H. H. Lee, Y. Park, Y. S. Kim and C. Kim, *Org. Electron.*, 2013, **14**, 100-104.
7. J. Xiong, J. Yang, B. Yang, C. Zhou, X. Hu, H. Xie, H. Huang and Y. Gao, *Org. Electron.*, 2014, **15**, 1745-1752.
8. M. Law, L. E. Greene, J. C. Johnson, R. Saykally and P. Yang, *Nat. Mater.*, 2005, **4**, 455-459.
9. Y. Bai, H. Yu, Z. Li, R. Amal, G. Q. Lu and L. Wang, *Adv. Mater.*, 2012, **24**, 5850-5856.
10. K. S. Leschkies, R. Divakar, J. Basu, E. Enache-Pommer, J. E. Boercker, C. B. Carter, U. R. Kortshagen, D. J. Norris and E. S. Aydil, *Nano Lett.*, 2007, **7**, 1793-1798.
11. Y. Ohsaki, N. Masaki, T. Kitamura, Y. Wada, T. Okamoto, T. Sekino, K. Niihara and S. Yanagida, *Phys. Chem. Chem. Phys.*, 2005, **7**, 4157-4163.
12. X. Wu, G. Q. Lu and L. Wang, *Energy Environ. Sci.*, 2011, **4**, 3565-3572.
13. A. Hadipour, D. Cheyns, P. Heremans and B. P. Rand, *Adv. Energy Mater.*, 2011, **1**, 930-935.
14. M. K. Nazeeruddin, R. Splivallo, P. Liska, P. Comte and M. Gratzel, *Chem. Commun.*, 2003, 1456-1457.
15. J.-H. Yoon, S.-R. Jang, R. Vittal, J. Lee and K.-J. Kim, *J. Photochem. Photobiol. A.*, 2006, **180**, 184-188.
16. K. Zilberberg, J. Meyer and T. Riedl, *J. Mater. Chem. C*, 2013, **1**, 4796-4815.
17. J. Huang, Z. G. Yin and Q. D. Zheng, *Energy Environ. Sci.*, 2011, **4**, 3861-3877.
18. K. Mahmood, B. S. Swain, G. S. Han, B. J. Kim and H. S. Jung, *ACS Appl. Mater. Interfaces*, 2014, **6**, 10028-10043.
19. H. Park, S. Chang, J. Jean, J. J. Cheng, P. T. Araujo, M. Wang, M. G. Bawendi, M. S. Dresselhaus, V. Bulovic, J. Kong and S. Gradecak, *Nano Lett.*, 2013, **13**, 233-239.
20. D.-H. Yoo, T. V. Cuong, S. Lee, W. S. Hwang, W. J. Yoo, C.-H. Hong and S. H. Hahn, *J. Phys. Chem. C*, 2014, **118**, 17638-17642.
21. T. Xu, S. Venkatesan, D. Galipeau and Q. Qiao, *Sol. Energy Mater. Sol. Cells*, 2013, **108**, 246-251.
22. L. Vayssieres, *Adv. Mater.*, 2003, **15**, 464-466.
23. J. H. Chen, C. Jang, S. Xiao, M. Ishigami and M. S. Fuhrer, *Nat. Nanotechnol.*,

2008, **3**, 206-209.
24. S. V. Morozov, K. S. Novoselov, M. I. Katsnelson, F. Schedin, D. C. Elias, J. A. Jaszczak and A. K. Geim, *Phys. Rev. Lett.*, 2008, **100**, 016602.
25. C. Gómez-Navarro, R. T. Weitz, A. M. Bittner, M. Scolari, A. Mews, M. Burghard and K. Kern, *Nano. Lett.*, 2007, **7**, 3499-3503.
26. D.-H. Yoo, T. V. Cuong, V. H. Luan, N. T. Khoa, E. J. Kim, S. H. Hur and S. H. Hahn, *J. Phys. Chem. C*, 2012, **116**, 7180-7184.
27. Y. J. Kim, H. Yoo, C. H. Lee, J. B. Park, H. Baek, M. Kim and G. C. Yi, *Adv. Mater.*, 2012, **24**, 5565-5569, 5564.
28. W. M. Choi, K. S. Shin, H. S. Lee, D. Choi, K. Kim, H. J. Shin, S. M. Yoon, J. Y. Choi and S. W. Kim, *Nano Res.*, 2011, **4**, 440-447.
29. C. Han, Z. Chen, N. Zhang, J. C. Colmenares and Y.-J. Xu, *Adv. Funct. Mater.*, 2015, **25**, 221-229.
30. C.-H. Hsieh, Y.-J. Cheng, P.-J. Li, C.-H. Chen, M. Dubosc, R.-M. Liang and C.-S. Hsu, *J. Am. Chem. Soc.*, 2010, **132**, 4887-4893.
31. T. Hu, L. Chen , K. Yuan and Y. Chen, *Chem. –Eur. J.*, 2014, **20**, 17178-17184.
32. W. S. Hummers and R. E. Offeman, *J. Am. Chem. Soc.*, 1958, **80**, 1339-1339.
33. S. Guo, S. Dong and E. Wang, *ACS Nano*, 2009, **4**, 547-555.
34. Y. Chen, H. Fu, L. Tan and Y. Shi, *J. Mater. Chem. C*, 2014, *3*, 828-835.
35. B. Neises and W. Steglich, *Angew. Chem. Int. Ed.*, 1978, **17**, 522-524.
36. L. E. Greene, M. Law, J. Goldberger, F. Kim, J. C. Johnson, Y. Zhang, R. J. Saykally and P. Yang, *Angew. Chem. Int. Ed.*, 2003, **42**, 3031-3034.
37. J. W. Jung, J. W. Jo and W. H. Jo, *Adv. Mater.*, 2011, **23**, 1782-1787.
38. X. W. M. Chen , Y. H. Yu , Z. L. Pei , X. D. Bai , C. Sun , R. F. Huang , and L. S., *Appl. Surf. Sci.*, 2000, *158*, 134-140.
39. D. Gao, J. Zhang, G. Yang, J. Zhang, Z. Shi, J. Qi, Z. Zhang and D. Xue, *J. Phys. Chem. C*, 2010, **114**, 13477-13481.
40. S. H. Liao, H. J. Jhuo, Y. S. Cheng and S. A. Chen, *Adv. Mater.*, 2013, **25**, 4766-4771.
41. J. Liqiang, W. Dejun, W. Baiqi, L. Shudan, X. Baifu, F. Honggang and S. Jiazhong, *J. Mol. Catal. A: Chem.*, 2006, **244**, 193-200.
42. G. Deroubaix and P. Marcus, *Surf. Interface Anal.*, 1992, **18**, 39-46.
43. P. Löfgren, A. Krozer, J. Lausmaa and B. Kasemo, *Surf. Sci.*, 1997, **370**, 277-292.
44. S. T. Tan, X. W. Sun, Z. G. Yu, P. Wu, G. Q. Lo and D. L. Kwong, *Appl. Phys. Lett.*, 2007, **91**, 072101.
45. M. P. Felicissimo, D. Jarzab, M. Gorgoi, M. Forster, U. Scherf, M. C. Scharber, S. Svensson, P. Rudolf and M. A. Loi, *J. Mater. Chem.*, 2009, **19**, 4899-4901.
46. I. Gonzalez-Valls and M. Lira-Cantu, *Energy Environ. Sci.*, 2009, **2**, 19-34.
47. H. Zeng, G. Duan, Y. Li, S. Yang, X. Xu and W. Cai, *Adv. Funct. Mater.*, 2010, **20**, 561-572.
48. K. Vanheusden, C. H. Seager, W. L. Warren, D. R. Tallant and J. A. Voigt, *Appl. Phys. Lett.*, 1996, **68**, 403-405.
49. S. B. Zhang, S. H. Wei and A. Zunger, *Phys. Rev. B*, 2001, **63**, 075205.

50. S. A. Studenikin, N. Golego and M. Cocivera, *J. Appl. Phys.*, 1998, **84**, 2287-2294.
51. J. H. Seo, R. Yang, J. Z. Brzezinski, B. Walker, G. C. Bazan and T.-Q. Nguyen, *Adv. Mater.*, 2009, **21**, 1006-1011.
52. S. Braun, W. R. Salaneck and M. Fahlman, *Adv. Mater.*, 2009, **21**, 1450-1472.
53. K. Woo, Y. Kim and J. Moon, *Energy Environ. Sci.*, 2012, **5**, 5340-5345.
54. T. B. Yang, M. Wang, C. H. Duan, X. W. Hu, L. Huang, J. B. Peng, F. Huang and X. Gong, *Energy Environ. Sci.*, 2012, **5**, 8208-8214.
55. H.-L. Yip, S. K. Hau, N. S. Baek, H. Ma and A. K. Y. Jen, *Adv. Mater.*, 2008, **20**, 2376-2382.
56. F. Zhang, M. Ceder and O. Inganäs, *Adv. Mater.*, 2007, **19**, 1835-1838.
57. J. S. Park, J. M. Lee, S. K. Hwang, S. H. Lee, H. J. Lee, B. R. Lee, H. I. Park, J. S. Kim, S. Yoo, M. H. Song and S. O. Kim, *J. Mater. Chem.*, 2012, **22**, 12695-12700.
58. H.-Y. Park, D. Lim, K.-D. Kim and S.-Y. Jang, *J. Mater. Chem. A*, 2013, **1**, 6327-6334.
59. X. Gong, M. Tong, F. G. Brunetti, J. Seo, Y. Sun, D. Moses, F. Wudl and A. J. Heeger, *Adv. Mater.*, 2011, **23**, 2272-2277.
60. J. C. Hummelen, B. W. Knight, F. LePeq, F. Wudl, J. Yao and C. L. Wilkins, *J. Org. Chem.*, 1995, **60**, 532-538.

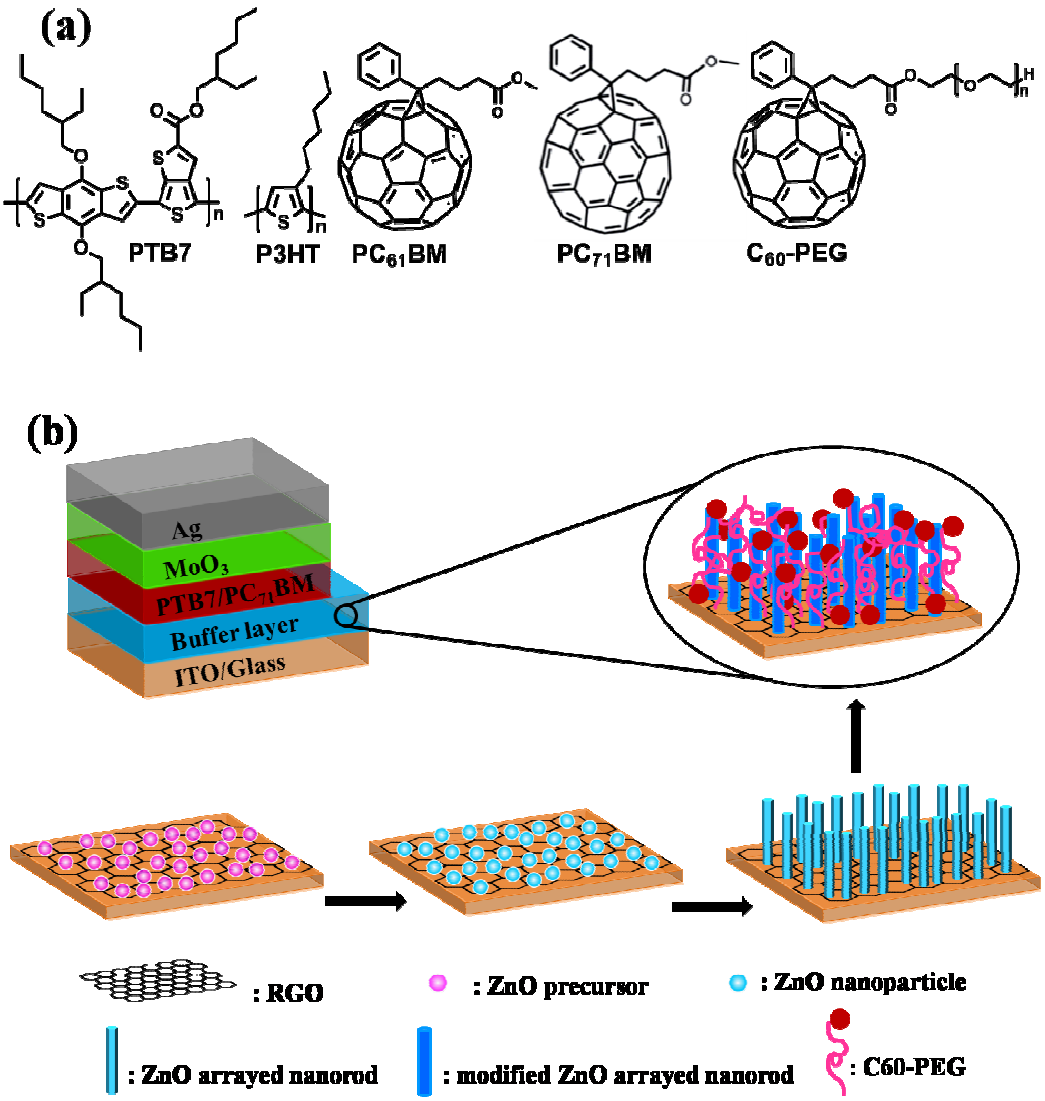

Figure 1. (a) Chemical structures of the materials used for device fabrication. (b) The structure of device and the schematic diagram of cathode buffer layer.

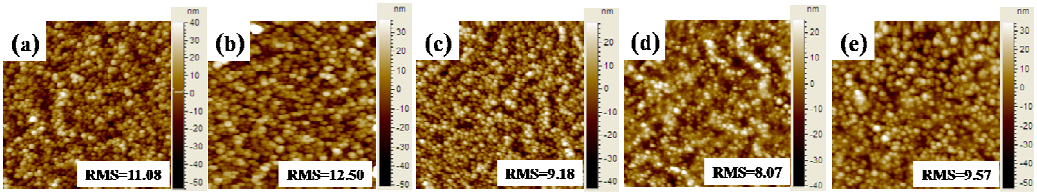

Figure 2. AFM height images (3μm×3μm) of (a) ZnO ANs, (b) C60-PEG/ZnO ANs, (c) ZnO ANs@RGO, (d) C60-PEG/ZnO ANs@RGO and (e) C60-PEG/ZnO ANs@RGO treated by plasma.

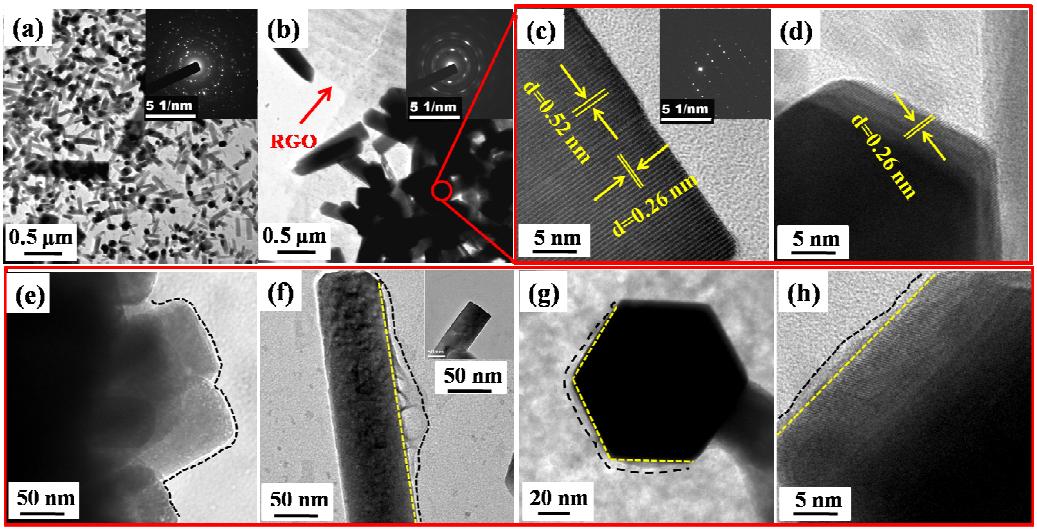

Figure 3. (a) TEM image of ZnO ANs and the inset is the SAED pattern of ZnO ANs. (b) TEM image of ZnO ANs@RGO and the inset is the SAED pattern of ZnO ANs in situ growing on graphene sheet. (c) and (d) HRTEM images of ZnO ANs@RGO and the inset in (c) is the SAED pattern of ZnO ANs. (e), (f) TEM micrograph of ZnO ANs@RGO modified by C60-PEG. The inset of (f) is the TEM image of ZnO ANs@RGO without C60-PEG. (g) TEM image and (h) HRTEM image of hexagonal ZnO ANs@RGO modified by C60-PEG.

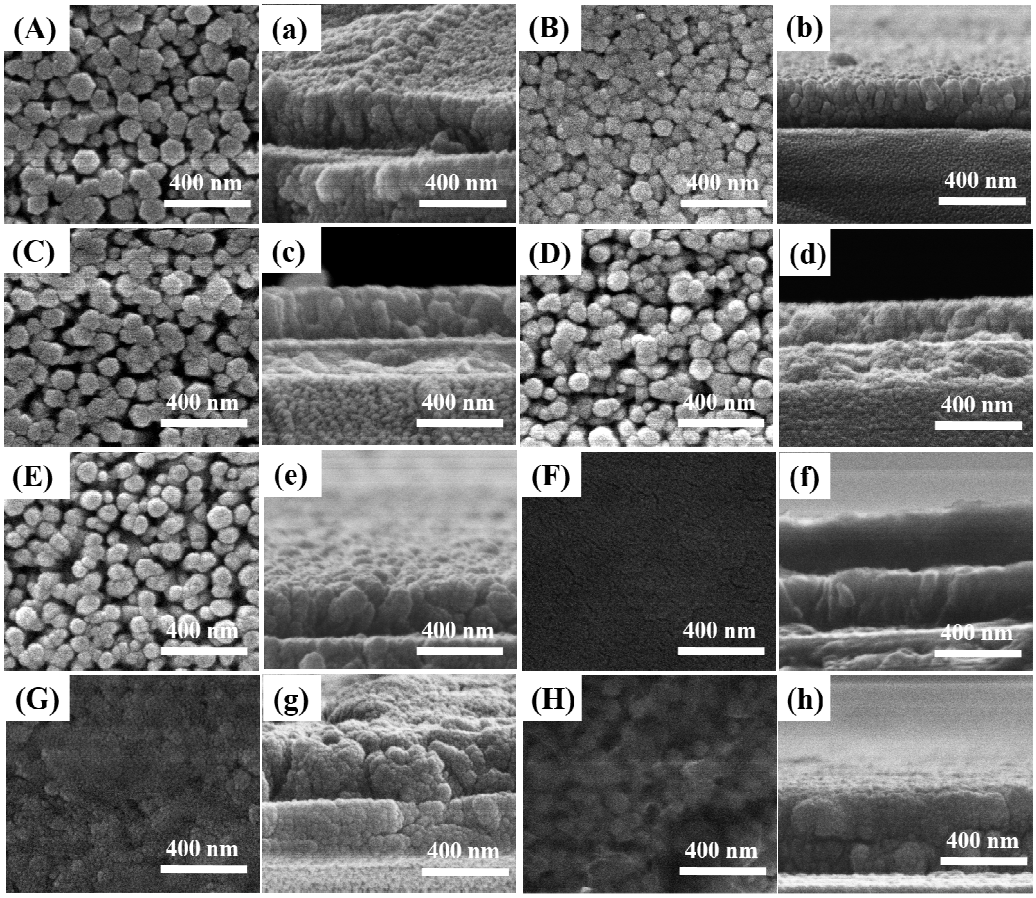

Figure 4. SEM top view and cross-section images of (A) ZnO ANs, (B) ZnO ANs modified by C60-PEG, (C) ZnO ANs@RGO, (D) ZnO ANs@RGO modified by C60-PEG, (E) ZnO ANs@RGO modified by C60-PEG and treated by plasma, (F) Active layer on C60-PEG/ZnO ANs, (G) Active layer on the top of C60-PEG/ZnO ANs@RGO, (H) Active layer on the top of C60-PEG/ZnO ANs@RGO treated by plasma. The image on the right of each SEM image is the corresponding cross-sectional SEM image.

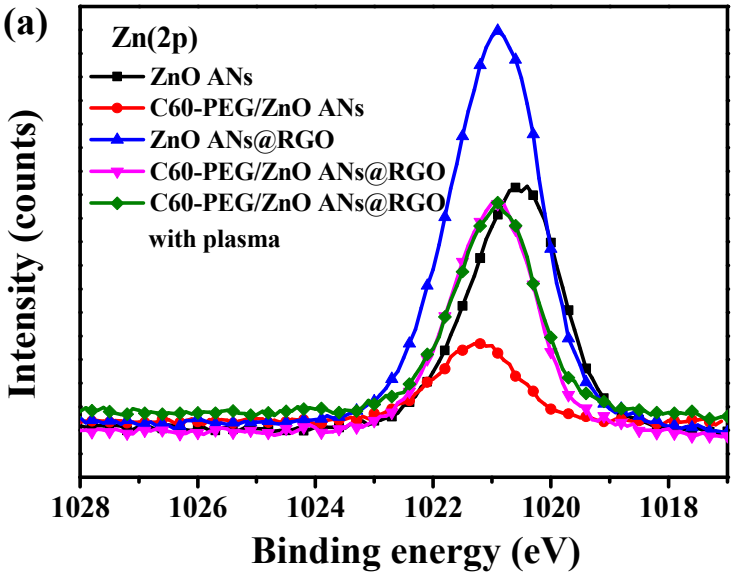

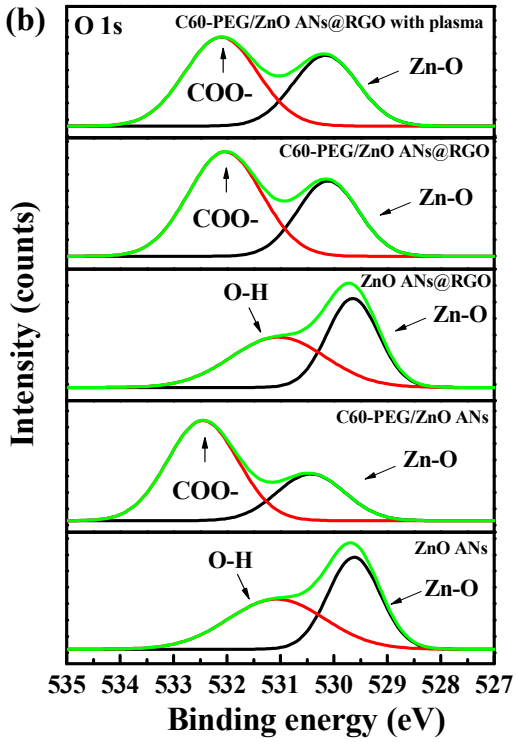

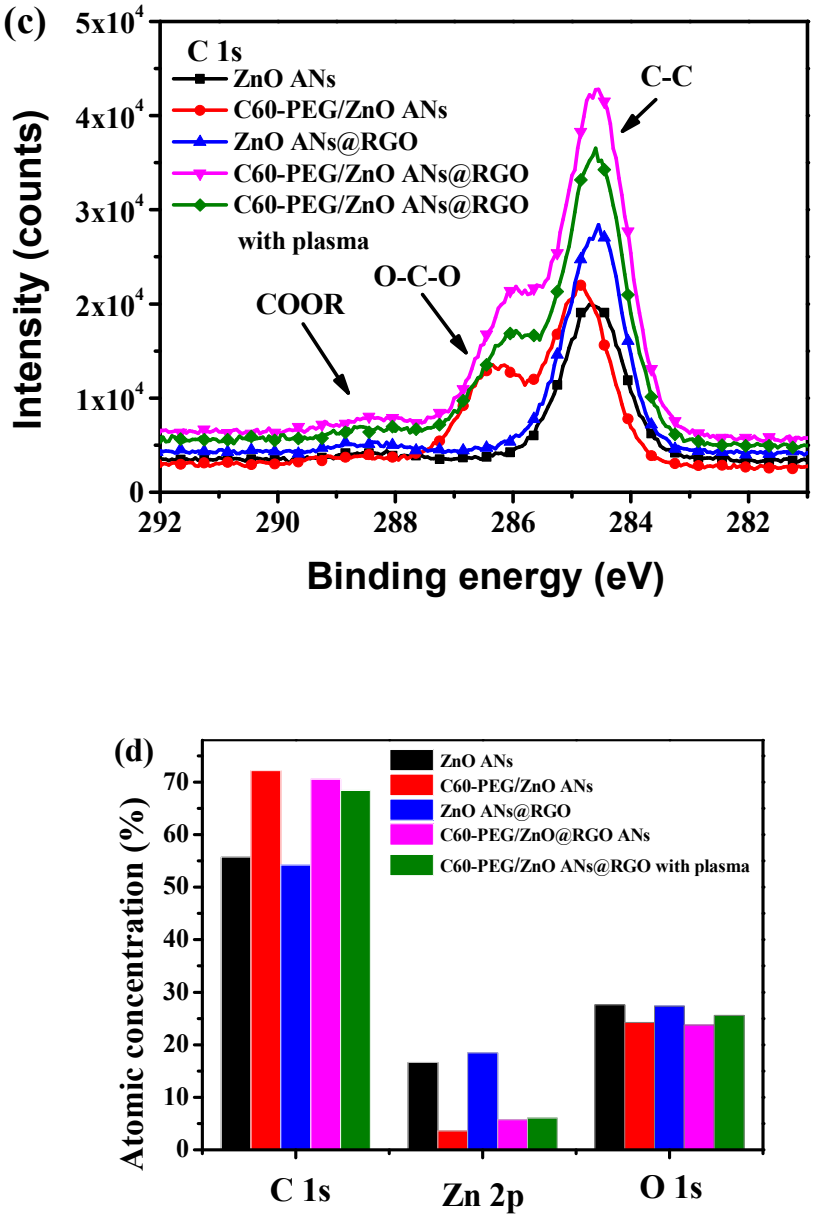

Figure 5. (a) Zn 2p, (b) O 1s and (c) C 1s XPS spectra of ZnO ANs, C60-PEG/ZnO ANs, ZnO ANs@RGO, C60-PEG/ZnO ANs@RGO and C60-PEG/ZnO ANs@RGO with plasma. (d) Atomic concentrations of carbon, zinc and oxygen based on the corresponding XPS spectra.

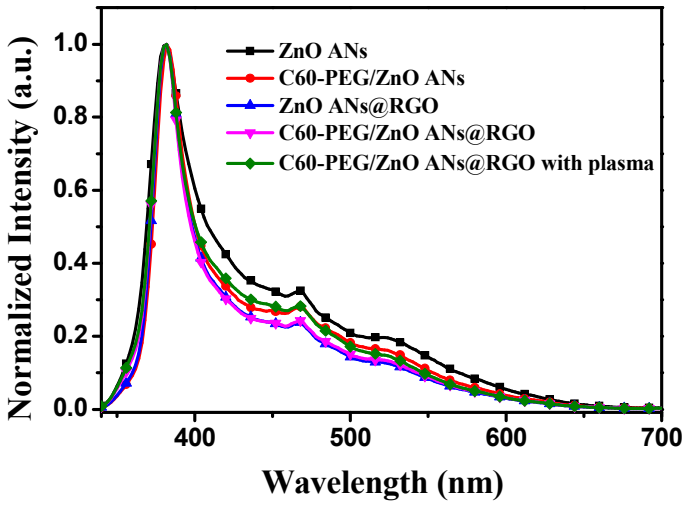

Figure 6. Normalized photoluminescence spectra of ZnO ANs, C60-PEG/ZnO ANs, ZnO ANs@RGO, C60-PEG/ZnO ANs@RGO and C60-PEG/ZnO ANs@RGO treated by plasma under photoexcitation at 325 nm.

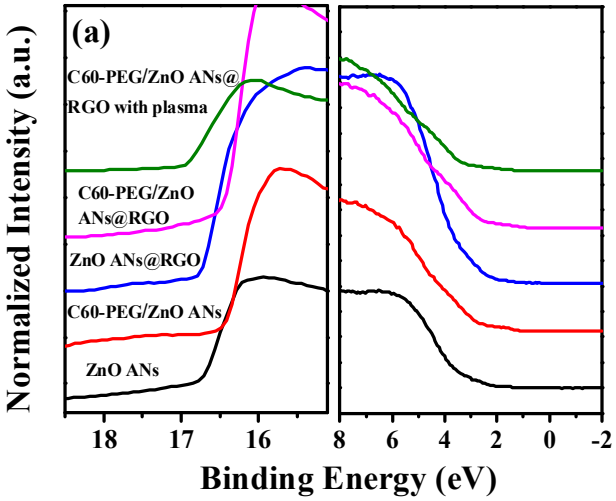

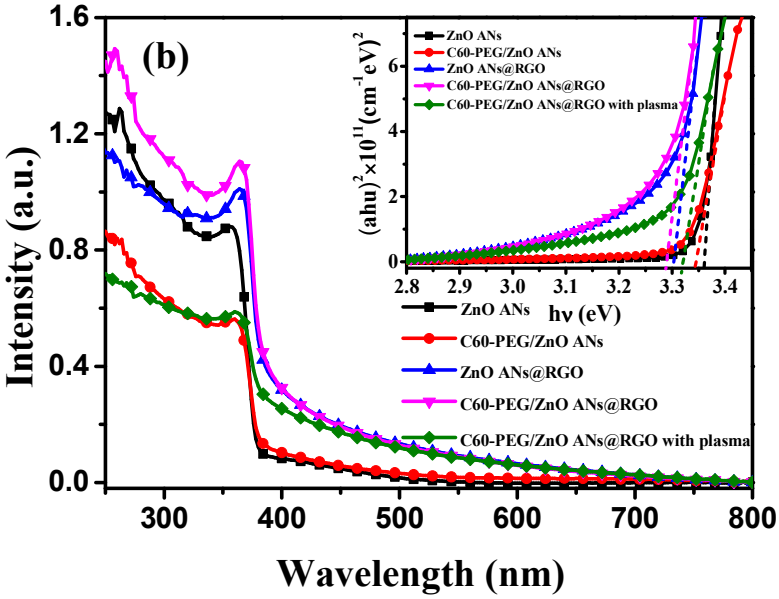

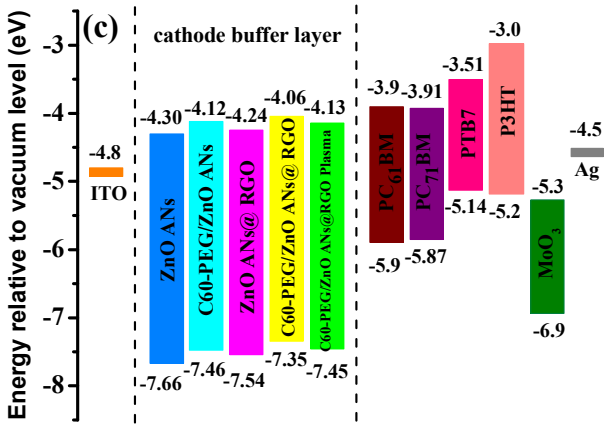

Figure 7. (a) UPS spectra and (b) UV–vis absorbance spectra (the inset is plots of $(\alpha hv)^2$ versus energy) of ZnO ANs, C60-PEG/ZnO ANs, ZnO ANs@RGO, C60-PEG/ZnO ANs@RGO and C60-PEG/ZnO ANs@RGO treated by plasma; (c) the corresponding energy level diagram of the components of the devices.

Table 1. Energy levels of ZnO ANs, C60-PEG/ZnO ANs, ZnO ANs@RGO, C60-PEG/ZnO ANs@RGO and C60-PEG/ZnO ANs@RGO treated by plasma.

Buffer layer	Eg (UV-Vis)	VB (UPS)	CB (Eg)
ZnO ANs	3.36	7.66	4.30
C60-PEG/ZnO ANs	3.34	7.46	4.12
ZnO ANs@RGO	3.30	7.54	4.24
C60-PEG/ZnO ANs@RGO	3.29	7.35	4.06
C60-PEG/ZnO ANs@RGO with plasma	3.32	7.45	4.13

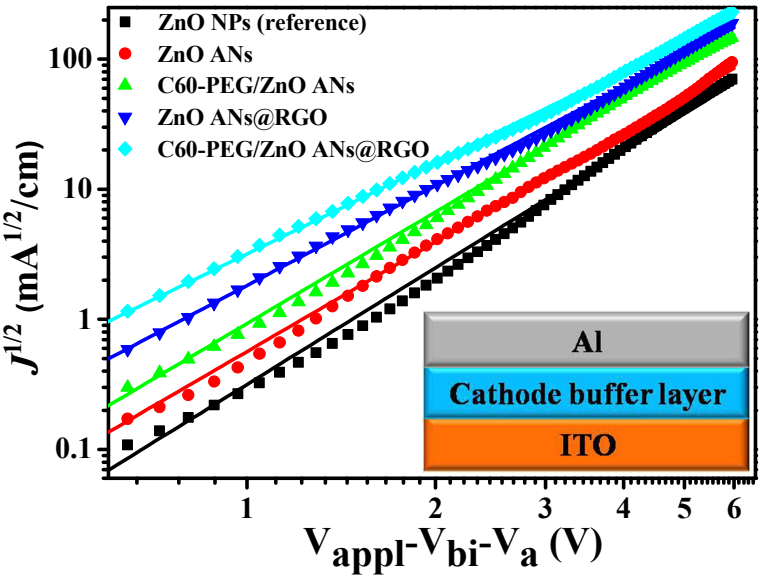

Figure 8. Log *J vs.* log *V* plots for Mott–Gurney SCLC fitting of the electron-only devices with a structure of ITO/cathode buffer layer/Al. Inset shows the configuration of the electron-only device.

Table 2. Electron mobility of devices with ITO/cathode buffer layer/Al structure by using (a) ZnO NPs, (b) ZnO ANs, (c) C60-PEG/ZnO ANs, (d) ZnO ANs@RGO, and (e) C60-PEG/ZnO ANs@RGO as cathode buffer layer.

Devices	a	b	c	d	**e**
μ_e ($cm^2\ V^{-1}\ s^{-1}$)	2.37×10^{-4}	3.63×10^{-4}	4.46×10^{-4}	7.32×10^{-4}	$\mathbf{9.56\times10^{-4}}$

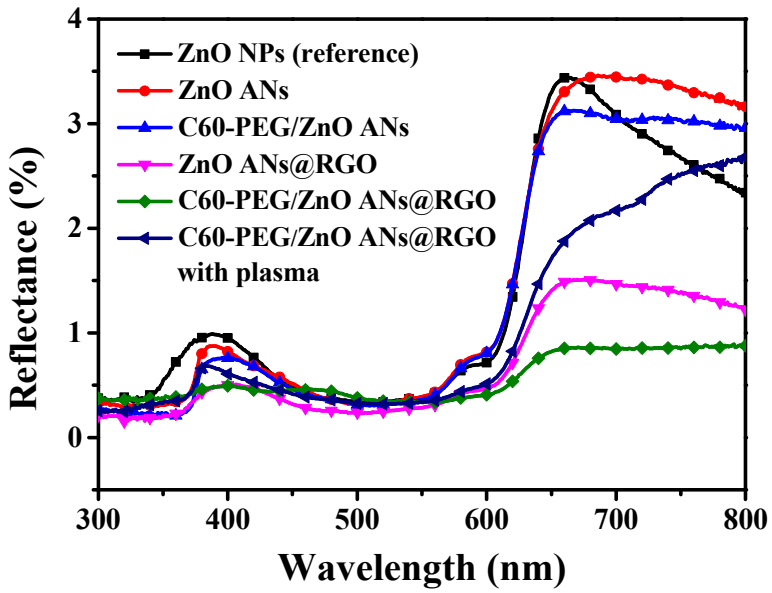

Figure 9. Diffuse reflectance spectra of the devices with ZnO NPs, ZnO ANs, C60-PEG/ZnO ANs, ZnO ANs@RGO, C60-PEG/ZnO ANs@RGO and C60-PEG/ZnO ANs @RGO treated by plasma as cathode buffer layer.

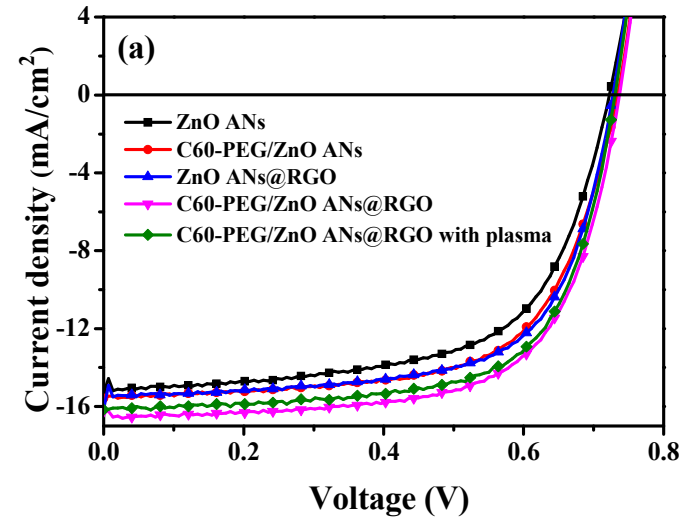

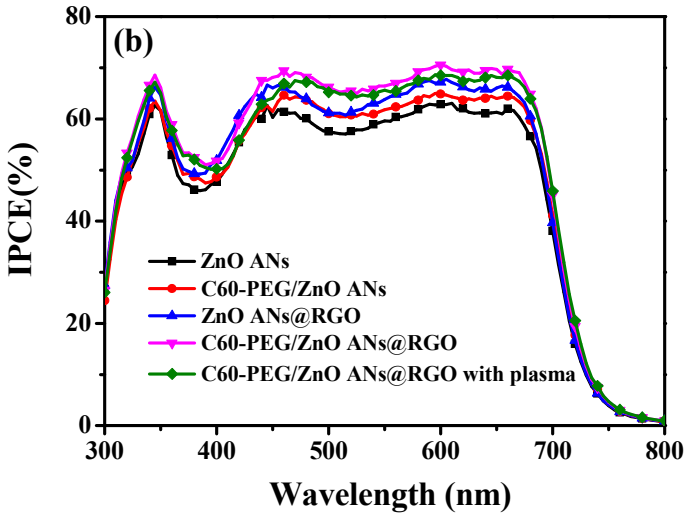

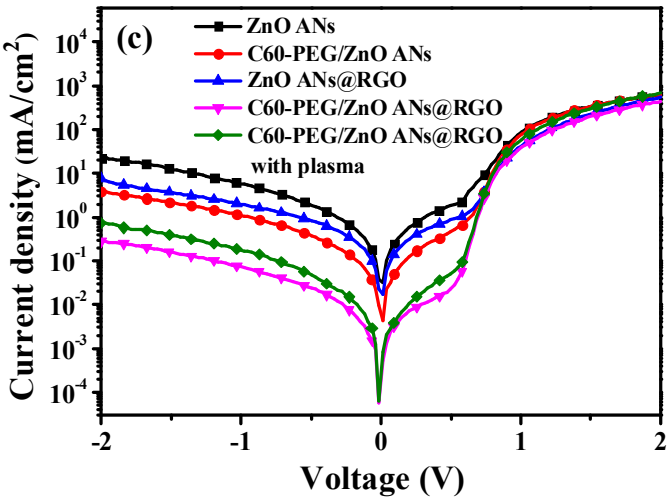

Figure 10. Performance of devices under simulated AM 1.5 G (100 mW·cm^{-2}) illumination. (a) Illuminated *J-V* characteristics, (b) IPCE spectra and (c) *J-V* curve under dark of the devices ITO/cathode buffer layer/PTB7:$PC_{71}BM$/MoO_3/Ag.

Table 3. Photovoltaic parameters of the devices with ITO/cathode buffer layer/PTB7:$PC_{71}BM$/MoO_3/Ag structure. (a) ZnO ANs, (b) C60-PEG/ZnO ANs, (c) ZnO ANs@RGO, (d) C60-PEG/ZnO ANs@RGO and (e) C60-PEG/ZnO ANs@RGO treated by plasma as cathode buffer layer.

Device	J_{sc} [mA cm^{-2}]	V_{oc} [V]	FF [%]	PCE [%]
a	15.31	0.721	62.0	6.9 ± 0.2
b	15.57	0.734	64.8	7.4± 0.2
c	16.13	0.727	63.9	7.5± 0.1
d	**16.25**	**0.737**	**67.7**	**8.1± 0.1**
e	16.15	0.730	67.2	7.9± 0.1

Highlights

Amphiphilic Fullerenes Modified 1D ZnO Arrayed Nanorods-2D Graphene Hybrids as Cathode Buffer Layers for Inverted Polymer Solar Cells

*Ting Hu, Lie Chen, Zhiqiang Deng, Yiwang Chen**

Amphiphilic fullerenes modified ZnO arrayed nanorods@RGO cathode buffer layer was developed to improve the performance of polymer solar cells.

Graphical abstract